12th International Symposium on Turbulence and Shear Flow Phenomena (TSFP12)
Osaka, Japan (Online), July 19-22, 2022

DNS STUDY OF TURBULENT FLOW THROUGH A CHANNEL ROUGHENED BY CIRCULAR-ARC RIBS

Weijian Xiong, Jinglei Xu
Jiangsu Province Key Laboratory of Aerospace Power System
Nanjing University of Aeronautics and Astronautics
Nanjing, 29th Yudao Street, China
xwj@nuaa.edu.cn, xujl@nuaa.edu.cn

S. V. Mahmoodi-Jezeh, Bing-Chen Wang
Department of Mechanical Engineering
University of Manitoba
Winnipeg, MB, R3T 5V6, Canada
mahmoosv@myumanitoba.ca, BingChen.Wang@umanitoba.ca

ABSTRACT

Turbulent flows through a channel roughened with circular-arc ribs of different pitch-to-height ratios (P/H = 3.0, 5.0 and 7.5) at a fixed Reynolds number of Re_b = 5600 are studied using direct numerical simulations (DNS). It is interesting to observe that in contrast to the classical channel flow with square bars, the flow separation point in a channel roughened with circular-arc ribs varies. The influences of the pitch-to-height ratio on the flow separation, statistical moments of the velocity field, budget balance of Reynolds stresses and anisotropy of turbulence stresses are investigated. The dynamics of coherent structures are studied by examining characteristics of the instantaneous velocity field, swirling strength and spatial-temporal two-point auto-correlations. It is also observed that the streamwise characteristic length of hairpin structures becomes increasingly shortened as the pitch-to-height ratio decreases.

INTRODUCTION

Turbulent boundary-layer flows over walls roughened by transverse circular-arc ribs have important applications to engineering problems, such as turbine blade cooling, heat exchangers and ship hull (Nagano *et al.* 2004). In this class of flows, large separation region arises from the continuous arc surfaces, and the position of the flow separation points is sensitive to the pitch-to-height ratio associated with eddy motions of different spatial and temporal scales. These features greatly complicate the flow physics, making turbulence characteristics considerably different from those of a classical 2-D rough-wall boundary-layer flow over a surface with square bars.

In the current literature, extensive experimental and numerical simulations are dedicated to investigations into the physics of 2-D rough-wall boundary-layer flows. Krogstad *et al.* (1992) studied the distributions of longitudinal turbulence intensity and Reynolds shear stresses over a rough wall in both inner and outer regions of a boundary layer. They showed that ejection and sweep events near the rough surface are dominant physical phenomena in terms of not only their intensity but also their frequency of occurrence. Krogstad *et al.* (1993) also conducted a wind-tunnel experiment to study the effects of the k-type roughness on the coherent structures of a turbulent boundary layer. They found that turbulence structures were massively influenced by the roughness in the outer region, which further led to a reduction in the streamwise characteristic length scales of the flow. For the d-type roughness flow, it is observed that most of the previous studies appearing in the literature utilitzed transverse square or triangular-shaped ribs (Coleman *et al.* 2007; Leonardi *et al.* 2007; MacDonald *et al.* 2018). For the square or triangle ribs, the flow separation is typically triggered by the sharp edges of ribs. This is in sharp contrast to the circular-arc ribs under current study, whose geometry is contoured continuously. Hence, the flow over circular-arc ribs exhibits a more complex separation behavior, which further affects the vortex dynamics and coherent flow structures of the turbulent boundary layer.

In view of these interesting physical features, we aim at performing a comprehensive high-fidelity DNS study of circular-arc-rib roughened channel flows of different pitch-to-height ratios. The results of the ribbed channel flows are compared against those of a smooth channel flow. Our study focuses on the effects of the pitch-to-height ratio on the position and characteristics of flow separation, statistical moments of the turbulent velocity field, budge balance of Reynolds stresses, as well as flow anisotropy. Also, we aim to investigate the characteristic scales and organization of coherent structures in the separation regions in both spatial and temporal spaces.

TEST CASE AND NUMERICAL ALGORITHM

Figure 1 shows the schematic diagram of the computational domain and coordinate system. Here, x, y and z denote the streamwise, wall-normal and spanwise coordinates, and u, v and w represent the corresponding velocity components, respectively. The streamwise length is set to $L_x = 6\delta$, where δ is the half channel height. In spanwise direction, the domain length is set to $L_z = 2\pi\delta$. The pitch and height of the circular-arc ribs are P and H, respectively. For all three ribbed channel flow cases considered, the radius of the arc is kept constant, i.e. $R = 0.2\delta$. Cases P1, P2 and P3 are compared here to investigate the effects of the pitch-to-height ratio (for P/H = 3.0, 5.0 and 7.5, respectively) with a common blockage ratio of $Br = H/2\delta = 0.1$. Due to the fixed domain size, cases P1, P2 and P3 consist of 10, 6 and 4 periods, respectively. The Reynolds number is fixed at $Re_b = 2\delta U_b/\nu = 5600$ to keep a constant mass flow rate, where U_b denotes the bulk mean

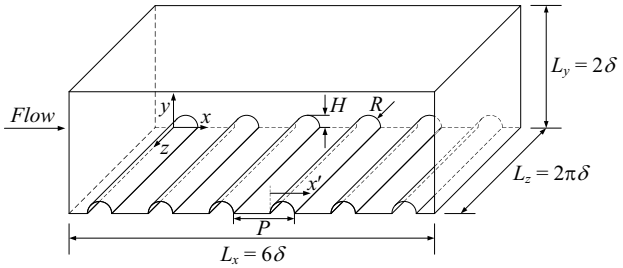

Figure 1. Schematic diagram of the computational domain and coordinate system. The origin of the absolute coordiante system $[x,y,z]$ is located at the inner bottom corner of the windward face of the first rib, and the origin of the relative streamwise coordinate x' is located at the windward face of each rib, which is defined to facilitate the analysis of a repeated rib period.

streamwise velocity. In order to identify the rib effects, an additional case of a smooth channel flow that follows Kim *et al.* (1987) has been simulated for the purpose of comparison. The flow field is fully developed and periodic boundary conditions are applied to both streamwise and spanwise directions. A no-slip boundary condition is imposed on all solid surfaces.

The DNS is performed using a spectral-element code so-called "Semtex" contributed by Blackburn & Sherwin (2004). This code is developed using C++ and FORTRAN programming languages, and parallelized using message passing interface (MPI) libraries. All physical quantities are expanded into the spectral space using Fourier series in the spanwise (z) direction, and 240 Fourier modes are used in each test case with a grid resolution of $5.3 \le \Delta_z^+ \le 5.9$ (measured in wall unit based on $u_{\tau S}$, the average friction velocity over the top smooth wall). Quadrilateral spectral-elements are used for discretization in the streamwise and vertical directions. For each element, a 4th-order Gauss-Lobatto-Legendre Lagrange polynomial is used. Case P3 has the finest grid resolution with $N_x \times N_y \times N_z = 1200 \times 161 \times 240$ nodes. The streamwise grid resolutions varies for $2.6 \le \Delta_x^+ \le 4.4$, and the maximum value of Δ_y^+ of the first grid off the walls is 0.20 in all tested cases. To satisfy the demanding requirement of DNS on grid resolutions, the ratio of the grid size over Kolmogorov scale η is limited to $2.17 \le \max(\Delta/\eta) \le 3.43$, where $\Delta = \sqrt[3]{\Delta_x \Delta_y \Delta_z}$. A second-order time-splitting scheme with three sub-steps is used for time integration. Overall, the discrete solution to the governing equations based on the Semtex code is highly accurate and the DNS results are of a spectral accuracy. The computer code has been used by our group for conducting DNS studies of rotating elliptical pipe flows (Rosas *et al.* 2021), and square channel flows (Fang *et al.* 2017).

For each simulated ribbed flow case, 600 instantaneous flow fields over 35 large-eddy turnover times (LETOTs, defined as $\delta/u_{\tau R}$) were used for collecting statistics once the flow becomes fully-developed and statistically stationary after a precursor simulation. Here, $u_{\tau R}$ denotes the average friction velocity over the bottom rib-roughened wall. The simulations were conducted using the WestGrid (Western Canada Research Grid) supercomputers, and approximately 4 TB data have been generated for all three simulated cases. For each test case, approximately 100,000 CPU hours were spent for solving the velocity field and for collecting the flow statistics.

RESULTS AND DISCUSSIONS

Table 1 summarizes key flow parameters for three ribbed flow cases. Here, two friction Reynolds numbers ($Re_{\tau R} = \delta u_{\tau R}/\nu$ and $Re_{\tau S} = \delta u_{\tau S}/\nu$) are defined based on the mean

Table 1. Geometry and flow parameters of the test cases

Test case	Re_b	$Re_{\tau R}$	$Re_{\tau S}$	C_{pR}	C_{fR}
P1	5600	288	208	0.0143	0.00539
P2	5600	369	222	0.0336	0.00181
P3	5600	406	227	0.0409	0.00177

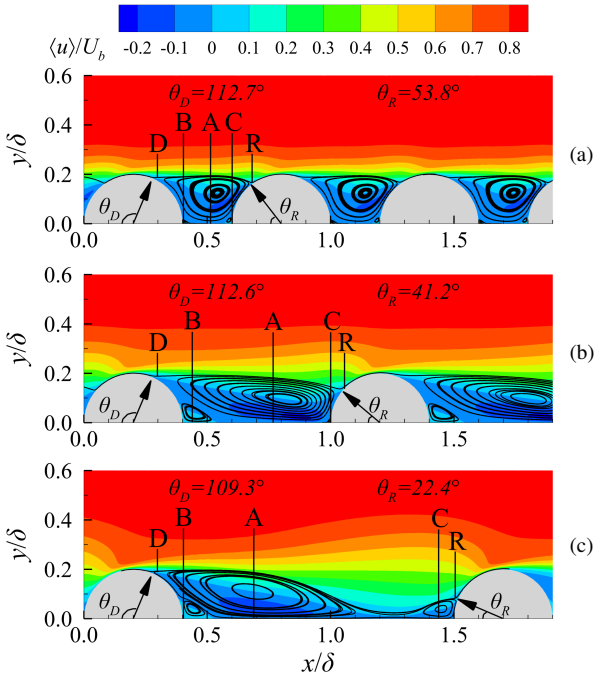

Figure 2. Time-averaged streamlines with contours of non-dimensional mean streamwise velocity $\langle u/U_b \rangle$ for all test cases. (a), (b) and (c) for cases P1, P2 and P3, respectively.

streamwise wall friction velocities of the roughened bottom wall and smooth top wall, respectively. The method for calculating the value of $u_{\tau R}$ follows the approach of Ismail *et al.* (2018) for a 2-D ribbed turbulent channel flow, viz. $u_{\tau R}^2 = D_p + D_\nu$. Here, D_p and D_ν are the mean pressure and viscous drags on the rough wall, determined as

$$D_p = \frac{1}{\rho L_x} \int_{\partial\Omega_R} \langle p \rangle dy \quad , \tag{1}$$

and

$$D_\nu = \frac{\nu}{L_x} \int_{\partial\Omega_R} \left[\left(\frac{\partial \langle u \rangle}{\partial y} + \frac{\partial \langle v \rangle}{\partial x} \right) dx - 2 \frac{\partial \langle u \rangle}{\partial x} dy \right] \quad , \tag{2}$$

respectively. In these equations, subscript '$\partial\Omega_R$' denotes the boundary of the rough bottom wall, and $\langle \cdot \rangle$ denotes averaging over time and over the spanwise direction. In table 1, the pressure and viscous drag coefficients are defined as $C_{pR} = D_p/(U_b^2/2)$ and $C_{fR} = D_\nu/(U_b^2/2)$, respectively, for the rough wall. From table 1, it is clear that as the pitch-to-height ratio increases from 3.0 to 7.5, both values of $Re_{\tau R}$ and $Re_{\tau S}$ increase monotonically, indicating an increase of friction drags on both sides of the channel. As the pitch-to-height ratio increases, it is interesting to observe that the trend of C_{pR} and C_{fR} is opposite of each other. Furthermore, the ratio of C_{pR} to C_{fR} increases monotonically, as a result of augmentation of the recirculation bubble size behind the ribs.

The mean flow structures of the test cases are shown in figure 2 using the contours of non-dimensional mean streamwise velocity $\langle u \rangle / U_b$ and the time-averaged streamlines. The significant mean flow vortices are marked with A, B and C,

which represent the large recirculation bubbles behind the ribs (A), the small secondary vortices located at the corners of the windward and leeward sides of the ribs (B and C, respectively). D and R indicate the detachment and reattachment points of the mean flow, respectively. Accordingly, θ_D and θ_R denote the angles corresponding to the positions of the detachment and reattachment points of the mean flow on the circular-arc ribs. The detachment (D) and reattachment (R) points are defined as the positions where the local mean wall shear stress vanishes, i.e. $\langle \tau_w \rangle = 0$. From figure 2, it is clear that with an increasing value of P/H, the reattachment point moves upstream progressively, while the detachment point is stable. As a result, the distance between points D and R increases monotonically and the flow accelerates near the rib crest as the pitch-to-height ratio increases. This leads to a larger pressure difference between the windward and leeward of a rib, which further increases the form drag dramatically. The mean flow pattern of case P3 discussed here is typical of the k-type rough-wall flow. For cases P1 and P2, the mean flow skims over the ribs, which is typical of a d-type rough-wall flow.

To assess the effect of the pitch-to-height ratio on the separation vortices, flow separation indicator introduced by Simpson (1981) can be studied, which is defined as

$$\gamma_p = \langle H(u) \rangle \quad , \tag{3}$$

where

$$H(u) = \begin{cases} 1, & \text{if } u > 0 \\ 0, & \text{otherwise} \end{cases} \tag{4}$$

is the unit step function of the instantaneous streamwise velocity u. The value of γ_p is calculated as the first grid off the rough bottom wall, and the flow features separation if $\gamma_p < 0.5$. Figure 3 shows the azimuthal and streamwise distribution of γ_p on the bottom wall. In figure 3(a), the reattachment and detachment points of the mean flow (R and D in figure 2, respectively) are marked using '$\diamond$' and '$\times$', respectively, and the incipient detachment (ID) points (where $\gamma_p = 0.99$) are marked using '$\triangle$'. The displacement thickness of the boundary layer begins to increase rapidly after the ID point (Simpson 1989). From figure 3(a), it is obvious that the values of γ_p for all cases are all above 0.5 at the reattachment point, which is in sharp contrast to that of the classical backward-facing step flow in which γ_p is less than 0.5 at the reattachment point (Simpson 1989). The value of γ_p over 0.5 at the reattachment point indicates the existence of a large-scale intermittent backward flow around this position due to the flow impingement on the rib. As the value of P/H increases, the value of γ_p at the reattachment point deviates from 0.5 gradually, showing the enhanced flow impingement onto the rib surface. With an increasing value of P/H, the ID point and detachment point of the mean flow both move upstream on the rib surface, and the backward flow becomes much weaker associated with the occurance of the lowest value of γ_p and the proportion of rib surface of $\gamma_p < 0.5$. Consequently, as the value of P/H increases, the angle between ID point and detachment point of the mean flow increases monotonically, which is $\Delta\theta = 9.49°$, 13.47° and 15.68° for cases P1, P2 and P3, respectively. It is understood that with a wider rib spacing, the turbulent motions becomes stronger and the separation events occur less intensively on the rib surface. From figure 3(b), it is apparent that there are two valleys in the profile of γ_p in case P3, corresponding to vortices A and C in figure 2(c). The peak located around $x'/\delta = 1.25$ between the two valleys results from a reattachment event. In cases P1 and P2, there is only one valley between two ribs, which corresponds to the large recirculation bubble. Compared to case P3, the secondary dettachment vortex C changes to a small reattachment vortex in cases P1

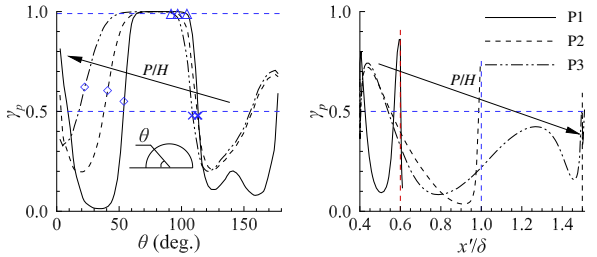

(a) profiles of γ_p along the rib surface (b) profiles of γ_p within the cavity between two ribs

Figure 3. Distribution of the mean flow separation indicator γ_p on the bottom wall. '$\diamond$', '$\times$' and '$\triangle$' in panel (a) denote the reattachment, detachment point of the mean flow and the incipient detachment point, respectively. The vertical red, blue and black dashed lines in panel (b) demarcate the windward corner of cases P1, P2 and P3, respectively.

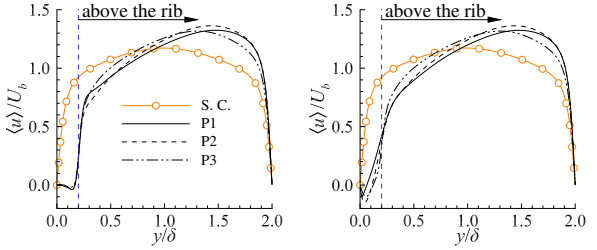

(a) profiles of $\langle u \rangle$ at the leeward of ribs ($x'/\delta = 0.4$) (b) profiles of $\langle u \rangle$ midway between ribs

Figure 4. Vertical profiles of non-dimensionalized mean streamwise velocity at the leeward of ribs and the midspan between two adjacent ribs. S. C. denotes the smooth channel test case.

and P2 (or, as the value of P/H decreases from 7.5 to 5.0 and 3.0). It is obvious that an increase of the pitch-to-height ratio enhances instantaneous reattachment events between the ribs remarkably.

Figure 4 shows the profiles of mean streamwise velocity at the leeward corner of ribs ($x'/\delta = 0.4$) and at the midspan between two adjacent ribs ($x'/\delta = 0.5$, 0.7 and 0.95 for cases P1, P2 and P3, respectively). It is observed that the peak of $\langle u \rangle$ move towards the top wall of the channel as the value of P/H increases, although the density of the roughness elements decreases simultaneously. Figure 5 shows the spatial distribution and profile of TKE. From figures 5(a) and (b), it is apparent that TKE is generated intensively in the shear layer and transported downstream. A wake region is observed after the flow in the shear layer impinges onto the downstream rib and rushes upward to the channel center. Owing to the presence of the shear layer and wake region, the profiles of TKE at the leeward corner exhibits a dual-peak pattern, as is evident in figure 5(c). The roughness elements enhance the TKE level dramatically in a monotonic manner as the value of P/H increases. Furthermore, the TKE level is significantly lower under the rib height compared with the smooth channel scenario.

The study of rib effect on the turbulence energy transfer can be refined by examining the transport equation of Reynolds stresses, which is expressed as

$$H_{ij} = P_{ij} + \Pi_{ij} - \varepsilon_{ij} + D_{ij} \quad , \tag{5}$$

where H_{ij}, P_{ij}, Π_{ij}, ε_{ij} and D_{ij} represent the convection, production, pressure-strain, viscous dissipation, and diffusion terms, respectively, defined as

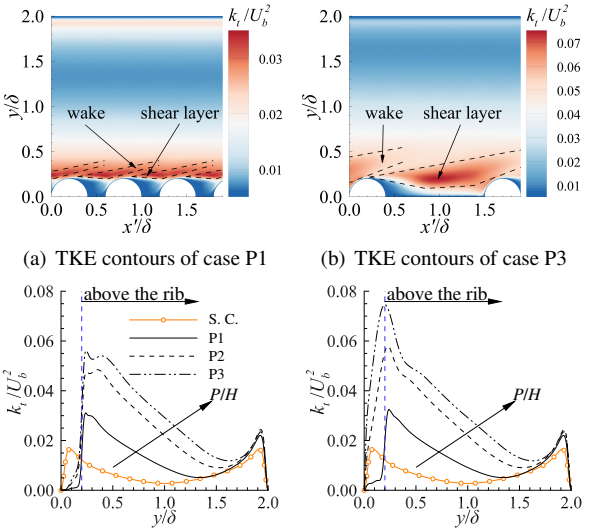

(a) TKE contours of case P1 (b) TKE contours of case P3

(c) profiles of TKE at the leeward of ribs (d) profiles of TKE at the midspan between two adjacent ribs

Figure 5. Contours and profiles of TKE at the leeward of ribs ($x'/\delta = 0.4$) and the midspan between two adjacent ribs ($x'/\delta = 0.5$, 0.7 and 0.95 for cases P1, P2 and P3, respectively). The vertical blue dashed lines demarcate the rib crest. S. C. denotes the smooth channel test case.

$$H_{ij} = \langle u_k \rangle \frac{\partial \langle u_i' u_j' \rangle}{\partial x_k} \quad , \tag{6}$$

$$P_{ij} = -\langle u_i' u_k' \rangle \frac{\partial \langle u_j' \rangle}{\partial x_k} - \langle u_j' u_k' \rangle \frac{\partial \langle u_i' \rangle}{\partial x_k} \quad , \tag{7}$$

$$\Pi_{ij} = \frac{1}{\rho} \left\langle p' \left(\frac{\partial u_i'}{\partial x_j} + \frac{\partial u_j'}{\partial x_i} \right) \right\rangle \quad , \tag{8}$$

$$\varepsilon_{ij} = 2\nu \left\langle \frac{\partial u_i'}{\partial x_k} \frac{\partial u_j'}{\partial x_k} \right\rangle \quad , \tag{9}$$

$$D_{ij} = -\frac{\partial \langle u_i' u_j' u_k' \rangle}{\partial x_k} - \frac{1}{\rho} \left(\frac{\partial \langle p' u_i' \rangle}{\partial x_j} + \frac{\partial \langle p' u_j' \rangle}{\partial x_i} \right) + \nu \frac{\partial^2 \langle u_i' u_j' \rangle}{\partial x_k \partial x_k} \quad , \tag{10}$$

respectively. Figure 6 shows the vertical profiles of the budget terms of $\langle u'u' \rangle$ at the leeward corner of ribs ($x'/\delta = 0.4$), non-dimensionalized by U_b^3/δ. Compared with the smooth channel flow, the magnitude of all the budget terms is greatly enlarged on the rough-wall side, as is evident in figures 6(b)-(d). A distinct difference in the bugdet terms between the smooth and roughened channels is that at the leeward corner of ribs, all the budget terms decay to zero at the wall as a result of the low turbulent fluctuation level in that region. In the shear layer sightly above the rib crest, the production term P_{11} enhances dramatically and becomes the dominant source of $\langle u'u' \rangle$. To balance the high level of prodution, the dissipation term ε_{11}, diffusion term D_{11} and pressure-strain term Π_{11} reach their minima as the sink terms in the same region. Furthermore, an M-shaped pattern of the convection term H_{11} is observed near the rib crest, indicating that the turbulence energy generated by the shear layer near the rib crest is spread both ways in the vertical direction and in the downstream region of the rib. The convection term H_{11} reaches its negative minimum value in the wake region (for $0.3 < y/\delta < 0.4$) above the rib, where the budget is balanced by P_{11} as the source term, and Π_{11}, and ε_{11} and D_{11} as the sink terms. By comparing figures 6(b)-(d) with

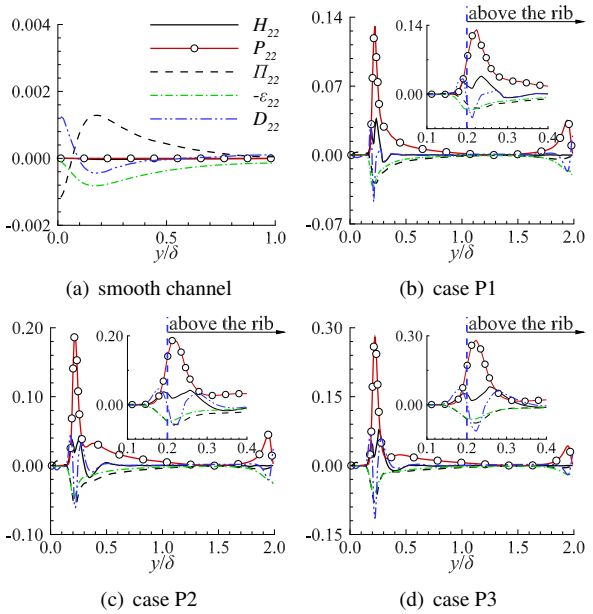

(a) smooth channel (b) case P1

(c) case P2 (d) case P3

Figure 6. Budget balance of $\langle u'u' \rangle$ at the leeward corner of ribs (x'/δ=0.4). All of the terms are non-dimensionalized by U_b^3/δ. The vertical blue dashed line demarcates the rib crest.

figure 6(a), it is evident that the budget balance near the smooth top wall of the ribbed flow cases is similar to that of the smooth channel flow. From figures 6(b)-(d), it is obvious that all budget terms enhance monotonically as the value of P/H increases. The magnitude of the diffusion term D_{11} is comparable to that of ε_{11} near the rib crest for the d-type roughness flow (or cases P1 and P2), but is greatly enhanced and becomes the dominant sink term in case P3 (at the highest P/H value tested).

To facilitate a deep understanding of the rib effects on flow anisotropy, the anisotropy invariant maps (AIM) introduced by Lumley & Newman (1977) are studied. AIMs provides an effective description of the local flow topologies associated with the Reynolds stress anisotropy tensor, defined as

$$b_{ij} = \frac{\langle u_i' u_j' \rangle}{\langle u_k' u_k' \rangle} - \frac{1}{3}\delta_{ij} \quad . \tag{11}$$

The Reynolds stress anisotropy tensor has three invariants as a second order tensor, one zero (i.e., $\mathrm{I} = b_{ii} = 0$) and two non-trial invariants (i.e., $\mathrm{II} = b_{ij}b_{ji}$ and $\mathrm{III} = b_{ij}b_{jk}b_{ki}$). There are three distinct characteristic states of turbulence associated with the so-called Lumley triangle: the axisymmetric turbulence state where one of the eigenvalue of the Reynolds stress tensor is either larger (III > 0) or smaller (III < 0) than the other two which are precisely equal in magnitude, and the two-component turbulence state in which one eigenvalue of the Reynolds stress tensor vanishes more rapidly than the other two.

Figure 7 compares the AIMs of the Reynolds stress anisotropy tensor at the leeward corner of the ribs ($x'/\delta = 0.4$) for the test cases. The AIMs in the top half of the channel for all cases are directly compared in figure 7(a). From figure 7(a), it is evident that the turbulence states of cases P1, P2 and P3 in the top half of the channel show a similar trend like the smooth channel flow, in the sense that a two-component turbulence state approaches the one-component turbulence state (II = 2/3 and III = 2/9) close to the wall, and becomes an axisymmetric turbulence state with a large eigenvalue in the log-law region owing to the rapid increase of $\langle u'u' \rangle$ in vertical direction. By comparing figures 7(b)-(d) with 8(a), it is seen that the shapes of AIMs in the bottom half of the channel are totally different due to the complex flow characteristics in the separation

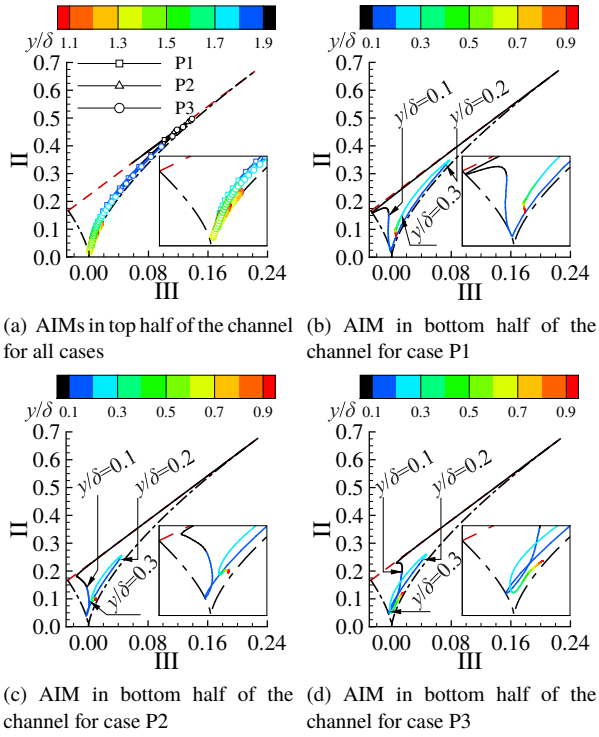

(a) AIMs in top half of the channel for all cases

(b) AIM in bottom half of the channel for case P1

(c) AIM in bottom half of the channel for case P2

(d) AIM in bottom half of the channel for case P3

Figure 7. Anisotropy invariant map based on II = $b_{ij}b_{ji}$ and III = $b_{ij}b_{jk}b_{ki}$ of the Reynolds stress anisotropy tensor at the leeward corner of the ribs (x'/δ=0.4) for the test cases. The dashed red line represents two-component turbulence state (defined as II = 2/9 + 2III), while the dash-dotted black line indicate axisymmetric turbulence state (defined as II = $6(\text{III}/6)^{2/3}$).

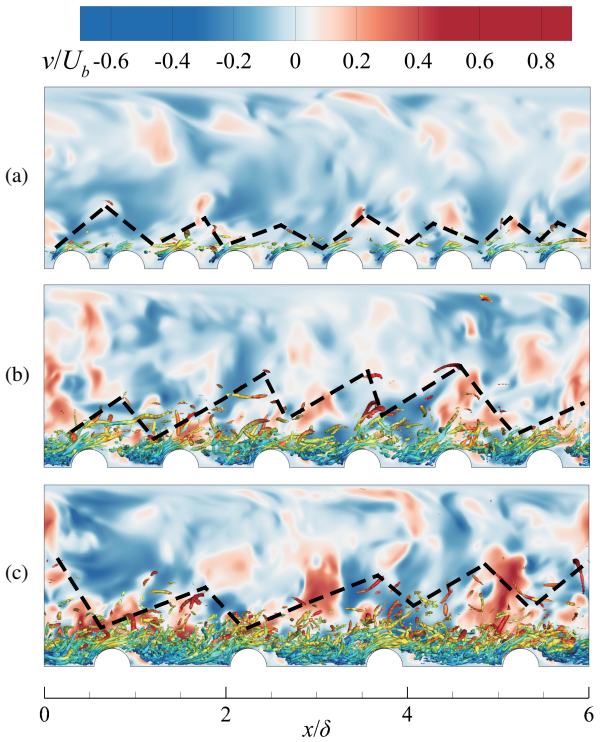

Figure 8. Iso-surface of swirling strength λ_{ci}, colored with non-dimensional instantaneous streamwise velocity u/U_b, with background contours of instantaneous vertical velocity v/U_b. (a), (b) and (c) for cases P1, P2 and P3, respectively.

region. At the leeward corner of a rib, the turbulence state near the ribbed bottom wall (for $0.0 < y/\delta < 0.1$) resembles a two-component turbulence state. In consequence of the interaction between secondary vortex B at the leeward corner and the recirculation bubble A (shown in figure 2), the flow with low momentum beneath the ribs is strongly mixed with the flow with higher momentum in the recirculation bubble, causing the flow to move towards an isotropic state near $y/\delta = 0.15$. From figures 7(b)-(d), the flow evolves rapidly towards the axisymmetric turbulence state with a large eigenvalue in the shear layer (around $y/\delta = 0.2$) due to the large magnitude of $\langle u'u' \rangle$ which is the dominant component of TKE, and then returns to a quasi isotropic state around $y/\delta = 0.3$ under the influence from the mixing of the shear layer flow with the bulk flow. It is understood that the flow mixing can effectively reduce the degree of flow anisotropy in the separation flow. By comparing figures 7(b)-(d), it is observed that with an increasing value of P/H, the flow anisotropy within and above the shear layer (above $y/\delta = 0.2$) is weakened, as a result of the enhanced interaction between the flow within the cavities between ribs and the outer bulk mean flow above them.

Figure 8 shows the iso-surface of the swirling strength λ_{ci} colored by the non-dimensionalized instantaneous streamwise velocity. The presence of hairpin structures are evident. In the figure, the heads of hairpin vortices with high momentum are intentionally connected with black dashed lines. Clearly, the intensity of turbulence motions becomes increasingly enhanced as the pitch-to-height ratio increases. The black dashed lines can be treated as the boundaries of the uniform momentum zones following Adrian *et al.* (2000). The quasi-periodic streamwise spacing between these dashed lines shows the size of the hairpin packets. The successive ejection and sweep events compose a burst event, which contributes greatly to the magnitude of Reynolds stresses. From figure 8, it is observed that with an increasing value of P/H, the hairpin packets are less likely to be broken up by the ribs, and more hairpins are conserved in a single packet, which increases the strength of uniform coherent motions and burst events, and further increases the level of Reynolds stresses.

The spatial-temporal features of coherent motions can be studied using the streamwise spatial-temporal two-point auto-correlations, defined as

$$R^{ts}_{uu}(x_r, y_r, \xi, \tau) = \frac{\langle u'(x_r, y_r, t_r) u'(x_r + \xi, y_r, t_r + \tau) \rangle}{\sqrt{\langle u'^2(x_r, y_r, t_{ref}) \rangle \langle u'^2(x_r + \xi, y_r, t_r + \tau) \rangle}}, \quad (12)$$

where subscript 'r' denotes the reference point. Figure 9 demonstrates the contours of R^{ts}_{uu} on the ξ-η phase plane. The reference points correspond to the peaks of TKE at the leeward corner of a rib (i.e., $[x'/\delta, y/\delta]$ = [0.4,0.24], [0.4, 0.25] and [0.4, 0.24] for cases P1, P2 and P3 in panels (a), (c) and (e), respectively) and the midpoint between two ribs (i.e., $[x'/\delta, y/\delta]$ = [0.5,0.24], [0.7, 0.23] and [0.95, 0.20] for cases P1, P2 and P3 in panels (b), (d) and (f), respectively). From figures 9(a) (c) and (e), it is clear that as the value of P/H increases, the isopleths become increasingly asymmetric about the origin as a result of the intensive interaction between the strong wake in the outer-layer from the previous rib period and the shear layer induced by the present rib. By comparing figures 9(a), (c) and (e) with (b), (d) and (f), it is evident that the size of the isopleths at the rib midspan is smaller than that at the leeward corner, showing a smaller spatial and temporal scales due to an increased turbulence level. As the value of P/H increases, the shape of the correlation structures becomes increasingly shortened and flattened. The streamwise convection

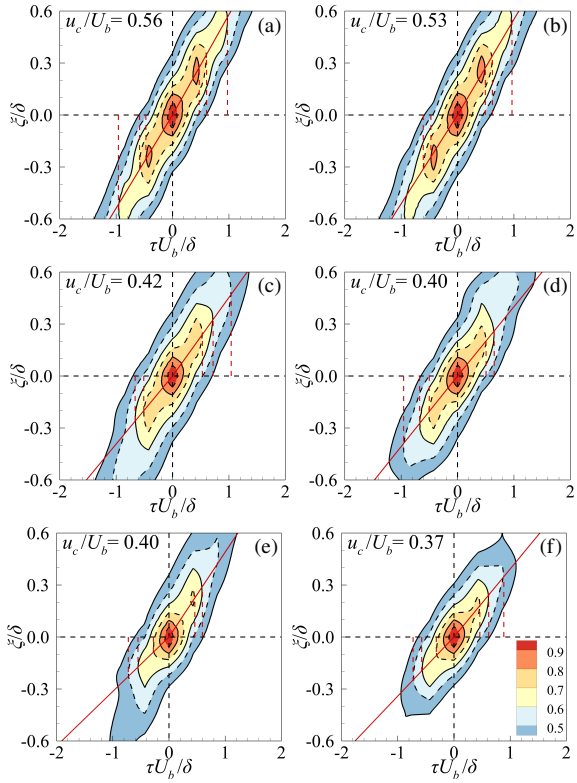

Figure 9. Contours of temporal and spatial two-point correlation coefficient R_{uu}^{ts} at the position corresponding to the peak value of TKE at the rib leeward and the rib midspan. (a), (c) and (e): leeward of ribs ($x'/\delta = 0.4$) for cases P1, P2 and P3; (b), (d) and (f): midspan between two adjacent ribs ($x'/\delta = 0.5$, 0.7 and 0.95) for cases P1, P2 and P3, respectively.

velocity $\langle u \rangle_c$ of the coherent structures can be calculated by the slope of the isopleths, which is marked using a red solid line in figure 9. It is interesting to see that the value of $\langle u \rangle_c$ decreases with an increasing value of P/H at both locations, though the TKE level is significantly enhanced. From figure 9, it is also observed that as the value of P/H increases, the characteristc spatial scale of coherent structures decreases remarkably while the characteristic time scale remains almost unchanged.

CONCLUSIONS

DNS of turbulence flows through a channel roughened with circular-arc ribs has been performed to investigate the pitch-to-height ratio (P/H) effect on the physics of flow separation, statistics of turbulent velocity field, and the characteristic scales of coherent structures. With a wider pitch between ribs, the reattachment point of the mean flow moves upstream progressively, while the detachment point remains stable, leading to an increase of the form drag on the rough-wall side. The angle between the incipient detachment point and the detachment point of the mean flow increases monotonically with an increasing value of P/H, indicating that the separation events become less intensive on the rib surface with an increased turbulence activities. It is also observed that an increase in the pitch-to-height ratio enhances the instantaneous reattachment events between two adjacent ribs remarkably.

Owing to the shear layer and wake region triggered by the ribs, the profiles of TKE at the leeward corner exhibits a dual-peak pattern. The presence of the rib elements enhances the magnitudes of TKE and budget terms of Reynolds stresses dramatically. The production term P_{11} increases significantly in the shear layer near the rib crest, which further augments $\langle u'u' \rangle$ dramatically near the rib-roughened wall. In the vicinity of the rib crest, $\langle u'u' \rangle$ is dominated by P_{11} as the source term, and by D_{11}, Π_{11} and ε_{11} as the sink terms. It is observed that the diffusion term D_{11} is greatly enhanced in the k-type roughness flow (case P3) with an increasing value of P/H. The AIMs of the Reynolds stress anisotropy tensor reveals that the mixing of the rib induced vortices and the bulk flow results in a remarkable reduction in the flow anisotropy. Furthermore, the flow over the rib crest tends to become isotropic as the value of P/H increases.

It is observed that as the pitch-to-height ratio P/H increases, the intensity of the turbulence motions enhances, and according to the distribution of the spatial-temporal two-point correlation R_{uu}^{ts}, the characteristic scale of coherent structures becomes increasingly shortened in the streamwise direction.

REFERENCES

Adrian, R. J., Meinhart, C. D. and Tomkins, C. D., 2000, "Vortex organization in the outer region of the turbulent boundary layer", *J. Fluid Mech.* **422**, 1-54.

Blackburn, H. M., and Sherwin, S. J., 2004, "Formulation of a Galerkin spectral element–fourier method for three-dimensional incompressible flows in cylindrical geometries", *J. Comp. Phys.* **197(2)**, 759–778.

Coleman, S. E., Nikora, V. I., Mclean, S. R. and Schlicke, E., 2007, "Spatially averaged turbulent flow over square ribs", *J. Eng. Mech.* **133(2)**, 194–204.

Fang, X., Yang, Z., Wang, B.-C., Bergstrom, D. J., 2017, "Direct numerical simulation of turbulent flow in a spanwise rotating square duct at high rotation numbers", *Int. J. Heat Fluid Flow* **63**, 88-98.

Ismail, U., Zaki, T. A. and Durbin, P. A., 2018, "Simulations of rib-roughened rough-to-smooth turbulent channel flows", *J. Fluid Mech.* **843**, 419-449.

Nagano, Y., Hattori H. and Houra, T., 2004, "DNS of velocity and thermal fields in turbulent channel flow with transverse-rib roughness", *Int. J. Heat Fluid Flow* **25**, 393-403.

Kim, J., Moin, P. and Moser, R., 1987, "Turbulence statistics in fully developed channel flow at low Reynolds number", *J. Fluid Mech.* **177**, 133-166.

Krogstad P.-Å., Antonia R. A. and Browne L., 1992, "Comparison between rough- and smooth-wall turbulent boundary layers", *J. Fluid Mech.* **245**, 599-617.

Krogstad, P.-Å., Antonia, R. A. and Browne, L. W. B., 1993, "The use of orthogonal X-wire arrays for structure investigation in a turbulent boundary layer", *Exp. Fluids* **15**, 231-239.

Leonardi, S., Orlandi, P. and Antonia, R. A., 2007, "Properties of d- and k-type roughness in a turbulent channel flow", *Phys. Fluids* **19**, 101-125.

Lumley, J. L. and Newman, G. R., 1977, " The return to isotropy of homogeneous turbulence", *J. Fluid Mech.* **82**(1), 161-178.

MacDonald, M., Ooi, A., García-Mayoral, R., Hutchins N. and Chung, D., 2018, "Direct simulation of high aspect ratio spanwise-aligned bars", *J. Fluid Mech.* **843**, 126-155.

Rosas, R. H., Zhang, Z.-P., Wang, B.-C., 2021, "Direct numerical simulation of turbulent elliptical pipe flow under system rotation about the major axis", *Phys. Rev. Fluids.* **6**, 084609.

Simpson, R. L., 1981, "A review of some phenomena in turbulent flow separation", *J. Fluids Eng.* **102**, 520-533.

Simpson, R. L., 1989, "Turbulent boundary-layer separation", *Ann. Rev. Fluid Mech.* **21**, 205-234.